HIGH RESOLUTION 3D DIFFUSION KURTOSIS IMAGING OF WHOLE RAT BRAIN

By

Nathaniel D. Kelm

Thesis

Submitted to the Faculty of the

Graduate School of Vanderbilt University

in partial fulfillment of the requirements

for the degree of

MASTER OF SCIENCE

in

Biomedical Engineering

May, 2014

Nashville, Tennessee

Approved:

Mark D. Does

Adam Anderson

ACKNOWLEDGEMENTS

I would like to thank my advisor, Dr. Mark Does, for his help and direction with this project as well as his continual support as a mentor. I would like to thank the rest of the Does lab group for their advice and assistance throughout the development of this project. Additionally, I would like to acknowledge my funding sources, NIH grant EB001744 and NIH T32 training grant EB014841, which made all of this work possible. Finally, I would like to thank my wife, Jessica, for her generous support and patience throughout this process.

TABLE OF CONTENTS

Page

LIST OF TABLES

LIST OF FIGURES

CHAPTER I

INTRODUCTION

I.1 Background and Motivation

I.1.1 Importance of Non-Invasive White Matter Imaging

Neuronal tissue in the central nervous system (CNS) is comprised of two main components: gray matter and white matter. Gray matter (so named because of its grayish appearance) is mainly composed of neuronal cell bodies, as well as glial cells, dendrites, and non-myelinated axons. White matter is mostly made up of myelinated axons, receiving its white coloring from the myelin sheaths wrapped around the axons. Myelin is an insulating lipid membrane wrapped in layers around axons of both the central and peripheral nervous systems that speeds up neuronal signal propagation along the axon as the signal jumps between non-myelinated sections called the nodes of Ranvier. Increases in axon diameter and the thickness of the myelin sheath each result in faster signal propagation along the nerve (1,2). Generally speaking, neuronal signals are generated and processed in gray matter and rapidly transported between different sections of the CNS through white matter axons.

There are many neurological diseases and disorders, such as multiple sclerosis (3) and schizophrenia (4), that are characterized by abnormalities in CNS white matter. Changes in white matter that may impede proper function include axonal injury, reduction in the number of axons, decrease in axon diameter, decrease in myelin

thickness, and abnormal myelin structure or development. Although histological evaluation of these abnormalities can provide accurate quantitative measures, this is mostly limited to a small, pre-selected region of tissue and is not practical for widespread research in humans. The ability to non-invasively detect and specify microstructural changes in white matter would have a tremendous clinical impact. Non-invasive imaging sensitive to changes in white matter is essential for the early diagnosis of white matter diseases and the development of treatments and therapies.

I.1.2 Diffusion MRI and White Matter

Since its first application in humans over 30 years ago, magnetic resonance imaging (MRI) has been widely used in the medical field due to its excellent soft-tissue contrast and high resolution. Diffusion-weighted MRI (DW-MRI) is an MRI method based upon the sensitization of the acquired MR signal to the motion or diffusion of water molecules. DW-MRI was first applied in the early 1990s for the early detection of cerebral ischemia or stroke (5,6). Even though this remains the most common clinical application of DW-MRI (7), DW-MRI has since gained momentum in the imaging of white matter. DW-MRI has shown promise in the detection and characterization of white matter diseases and disorders, including multiple sclerosis (8,9), schizophrenia (10), autism (11), and Alzheimer's disease (12).

Diffusion tensor imaging (DTI) is a rapidly developing quantitative DW-MRI method that characterizes the anisotropy of water diffusion in tissue, making it especially useful in white matter due to the parallel alignment of axons in bundles (13-17). Diffusion kurtosis imaging (DKI) is an extension of DTI with the potential of providing

additional information regarding white matter microstructure, including its state of myelination (18-22). Since its development, DKI has shown promising results in characterizing white matter changes in multiple diseases and disorders, including schizophrenia (23) and ADHD (24). Although further research and application is necessary, DKI could provide increased sensitivity and specificity to white matter microstructure compared with currently feasible clinical MRI protocols.

Prior to this work, DKI in rodent brains (both in vivo and ex vivo) has been limited to 2D multi-slice acquisitions (21). While this is capable of providing high in-plane resolution for distinguishing white matter tracts, the through-plane resolution is much lower and partial-volume averaging of white matter structures with their surroundings becomes a potential issue. Not only could this result in inaccurate DKI measures in "white matter" voxels, but also, sensitivity to white matter pathologies could decrease. Additionally, SNR is inherently lower for a 2D acquisition, reducing the precision of DKI-derived metrics. A high-resolution 3D acquisition with isotropic resolution could potentially alleviate these issues.

The purpose of this work includes the development of a DKI protocol for overnight, high-resolution 3D ex vivo rodent brain imaging. With high, isotropic resolution, partial-volume averaging of white matter tracts would be reduced and the high SNR available with a 3D acquisition would increase the precision of DKI measures. Application of this protocol will aid in the evaluation of rodent models of neurological disorders and diseases as well as in the assessment of the relationship between DKI-derived metrics and white matter microstructure.

I.2 Basics of Diffusion MRI

I.2.1 Molecular Diffusion of Water

The diffusion of water is characterized by random or Brownian motion of water molecules. First theorized by Albert Einstein, there exists a relationship between the diffusion coefficient of a liquid and the root-mean-squared displacement of molecules in the liquid during a given amount of time. This relationship, known as the Einstein equation for diffusion, is defined as:

$$x_{rms} = \sqrt{2Dt}, \quad [1]$$

where x_{rms} is the 1D root-mean-squared displacement, D is the diffusion coefficient in units of distance squared per time, and t is the diffusion time (25). In an unrestricted medium, the diffusion of water molecules can also be described by a Gaussian probability density function $P(x, t)$:

$$P(x, t) = (4\pi Dt)^{-\frac{3}{2}} \exp\left(-\frac{x^2}{4Dt}\right). \quad [2]$$

However, when considering water diffusion in biological tissue, this does not hold true. Barriers such as organelles, cell membranes, macromolecules, and other cellular structures hinder water diffusion, causing a reduction in the apparent diffusion coefficient of water and a deviation from a pure Gaussian diffusion displacement PDF (26). Because of this phenomenon, changes in the apparent water diffusion coefficient in biological tissues can provide insight into the underlying tissue microstructure.

I.2.2 Diffusion MRI Signal and PGSE

The idea of measuring water diffusion using nuclear magnetic resonance (NMR) existed long before the development of the modern MRI scanner. Through NMR experiments during the 1950s, it was discovered that the diffusion of water molecules in the presence of a magnetic field gradient (or spatially-varying magnetic field) causes a phase dispersion of the transverse magnetization and a resulting attenuation of NMR signal (27). Therefore, the same magnetic field gradients that are used for spatial encoding in conventional MRI experiments can also be used to indirectly measure the diffusion of water through signal attenuation or "diffusion weighting."

Although the magnetic field gradients can be applied in a variety of different ways to cause diffusion weighting of the signal, the most common method is the pulsed gradient spin-echo (PGSE) introduced by Stejskal and Tanner in 1965 (28) shown in Figure 1. This method utilizes two diffusion-weighting gradient pulses equal in area: the first induces a spatially dependent phase shift on the magnetic spins along the direction of

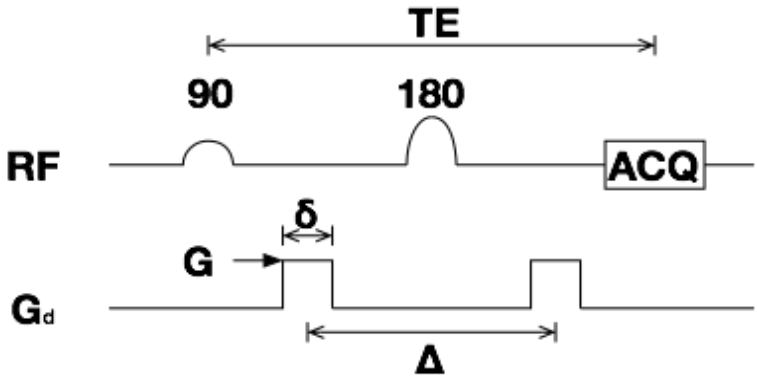

Figure 1. PGSE pulse sequence. Similar to a conventional spin-echo pulse sequence, spins are excited by the 90-degree RF pulse, refocused by the 180-degree pulse, and the echo signal is acquired at the echo time, TE. Diffusion-weighting gradient pulses with amplitude G and duration δ are added on both sides of the 180-degree pulse, separated by a diffusion time Δ.

the applied gradient and the second rewinds this shift. The diffusion of water molecules during the time between the two pulses along the same direction of the applied gradient pulses will cause a phase accumulation ϕ that is proportional to the displacement of the molecules:

$$\phi = \gamma \int_0^t \vec{G}(t')\vec{r}(t')dt', \quad [3]$$

where γ is the gyromagnetic ratio, $\vec{G}(t)$ is the magnetic field gradient and $\vec{r}(t)$ is the location of the magnetic spins. As noted earlier, in the case of unrestricted diffusion, the diffusion displacement of spins can be described by a Gaussian probability density function (PDF). Due to the diffusing spins having different displacements, and therefore different phases, within a given voxel, the MRI signal will be attenuated and the attenuation will be related to the variance of the Gaussian phase PDF, $< \phi^2 >$:

$$S = S_0 \exp(-< \phi^2 >), \quad [4]$$

where S is the acquired signal and S_0 is the signal without diffusion weighting. The relationship between the signal and the diffusion coefficient D follows:

$$S = S_0 \exp\left(-D\gamma^2 \int_0^{TE} \left[\int_0^t G(t')dt'\right]^2\right) = S_0 \exp(-bD), \quad [5]$$

where

$$b = \gamma^2 \int_0^{TE} \left[\int_0^t G(t')dt' \right]^2 . \quad [6]$$

b or the b-value is essentially the amount of diffusion weighting imparted by magnetic field gradients throughout the pulse sequence. Assuming rectangular diffusion gradient lobes and negligible imaging and background gradients, the b-value for a PGSE pulse sequence is:

$$b = \gamma^2 G^2 \delta^2 (\Delta - \frac{\delta}{3}), \quad [7]$$

where G is the diffusion gradient amplitude, δ is the gradient duration, and Δ is the gradient separation or diffusion time.

From Eq. 5, it is apparent that the diffusion-weighted signal is a function of the b-value, which is set by choosing values for the pulse sequence parameters G, δ, and Δ. Since b is determined by the acquisition parameters, Eq. 5 contains two unknown variables: S_0 and D. Therefore, estimating S_0 and D requires at least two acquisitions with different b-values (conventionally one image without diffusion weighting or "b=0" and one with diffusion weighting). Although useful qualitative information may be gained through a single diffusion-weighted image (such as in stroke), most diffusion MRI applications include the quantitative measurement of D using the above method.

I.2.3 Anisotropic Diffusion and the Diffusion Tensor

In biological tissue, not only do restrictions cause the diffusion displacement PDF to become non-Gaussian, but they also cause the apparent water diffusion to be anisotropic. This anisotropy is especially prominent in white matter where axons are aligned parallel to each other in bundles. Over diffusion times used in conventional DW-MRI experiments, water inside the axons moves further along the length of the axon than it does perpendicular to the axon. Axonal membranes and myelin act as barriers to the diffusion of water perpendicular to the axon. If these axons are aligned with one another within a given imaging voxel, then the measured water diffusion will be highly anisotropic.

As previously noted, diffusion gradients sensitize the MRI signal to water diffusion along a single direction. Therefore, if water diffusion is anisotropic, then the measured diffusion coefficient will change depending upon the direction. Generally, in white matter, this means that the measured diffusion coefficient will be greatest in the direction parallel to the axons within a given voxel. Determining the directional dependence of the diffusion of water could provide useful information regarding white matter microstructure and forms the basis of what is known as DTI.

In order to appropriately quantify orientation-dependent water diffusion, a 3D Gaussian model of displacements is needed. As opposed to using a single scalar diffusion coefficient, a symmetric, rank-2 diffusion tensor **D** or DT is used to characterize the diffusion along each axis (x, y, and z) as well as correlations between the diffusion on each axis (xy, xz, and yz) (13):

$$\boldsymbol{D} = \begin{bmatrix} D_{xx} & D_{xy} & D_{xz} \\ D_{xy} & D_{yy} & D_{yz} \\ D_{xz} & D_{yz} & D_{zz} \end{bmatrix}. \quad [8]$$

Since the tensor is symmetric, there are a total of 6 unique elements. In order to estimate **D**, diffusion coefficients along at least 6 non-collinear, non-coplanar directions must be calculated. Taking into account that at least 2 b-values are needed to estimate each diffusion coefficient, the minimum number of acquisitions required for DTI is 7 (1 b=0 and non-zero b-value along 6 different directions). The number of images acquired may be much greater than this if more b-values are needed for a better estimate of each diffusion coefficient or if more directions are desired to provide a better estimate of **D**. One way to calculate **D** from the diffusion coefficients is through the equation:

$$D(\boldsymbol{n}) = \sum_{i,j=1}^{3} n_i n_j \, \boldsymbol{D}_{ij}, \quad [9]$$

where $D(\boldsymbol{n})$ is the diffusion coefficient along a single direction and n_i is a normalized diffusion gradient component for each direction.

Once the diffusion tensor is estimated, it can be diagonalized so that rotationally invariant parameters can be calculated:

$$\boldsymbol{D} = \begin{bmatrix} \lambda_1 & & \\ & \lambda_2 & \\ & & \lambda_3 \end{bmatrix}, \quad [10]$$

where λ_1, λ_2, and λ_3 are the eigenvalues with corresponding eigenvectors ε_1, ε_2, and ε_3. If we consider the rms diffusion displacement in a 3D case, then this can be described by

a “diffusion ellipsoid.” If the diffusion is isotropic, then the ellipsoid is spherical; if diffusion is anisotropic, then the ellipsoid will be prolate or oblate. The axes of the ellipsoid are aligned with the eigenvectors ε_1, ε_2, and ε_3 and the size of the ellipsoid corresponds with the eigenvalues λ_1, λ_2, and λ_3. By convention, the eigenvalues are sorted from highest to lowest so that λ_1 corresponds with the principal direction of diffusion. In the case of white matter DTI, it is generally assumed that the direction described by ε_1 is parallel to the axons within each voxel, since it corresponds to the direction of highest diffusion. This convention has led to the method of DTI tractography, in which nerve fibers in the brain are mapped out according to the direction of the principal eigenvector (29,30).

From the eigenvalues, useful scalar DTI indices, including mean diffusivity, axial diffusivity, radial diffusivity, and fractional anisotropy, can be calculated. Mean diffusivity or MD describes the average diffusion coefficient over all directions and can be calculated by taking the mean of the eigenvalues:

$$MD = (\lambda_1 + \lambda_2 + \lambda_3)/3. \quad [11]$$

Axial diffusivity (AD) is diffusion along the principal diffusion direction and radial diffusivity (RD) is the average of diffusion along the other two axes:

$$AD = \lambda_1 \quad [12]$$

and

$$RD = (\lambda_2 + \lambda_3)/2. \quad [13]$$

Fractional anisotropy is a dimensionless metric ranging in value from 0 to 1 that characterizes the level of diffusion anisotropy present in a voxel, with 0 being completely isotropic and 1 being completely anisotropic (31):

$$FA = \sqrt{\frac{3}{2}}\frac{\sqrt{(\lambda_1 - MD)^2 + (\lambda_2 - MD)^2 + (\lambda_3 - MD)^2}}{\sqrt{\lambda_1^2 + \lambda_2^2 + \lambda_3^2}}. \quad [14]$$

Despite an inherent lack of specificity, combinations of MD, AD, RD, and FA are commonly used to evaluate white matter microstructure and have been shown to be sensitive to various white matter pathologies. Even though it is still based on the Gaussian diffusion assumption, the DTI model has seen widespread use and is still a highly researched topic.

I.3 Diffusion Kurtosis Imaging

I.3.1 Relationship Between Kurtosis and the Diffusion MRI Signal

Kurtosis is a dimensionless statistical metric that characterizes the sharpness of a distribution compared to a Gaussian distribution (32). The kurtosis K of a distribution is defined by the equation:

$$K = \frac{M_4}{M_2^2} - 3, \quad [15]$$

where M_N is the nth moment of the distribution about its mean. For a purely Gaussian distribution, $K = 0$. A positive kurtosis (leptokurtic) means that the distribution is more

peaked and has heavier tails compared with a Gaussian, whereas a negative kurtosis (platykurtic) means that the distribution is less peaked with less weight on its tails. Basically, the kurtosis can be used to characterize the non-Gaussianity of a distribution. Figure 2 demonstrates how changing the kurtosis can affect the shape of a distribution. As described previously, in the case of unrestricted diffusion, the water diffusion displacement PDF is strictly Gaussian. However, in biological tissue, water diffusion is no longer unrestricted and the displacement PDF becomes non-Gaussian. In nearly all cases, tissue will have a water diffusion kurtosis greater than 0, or a more peaked distribution than Gaussian. Measurement of the kurtosis of the water diffusion PDF could provide useful information with regards to the underlying tissue microstructure.

As stated before, Eq. 5 holds true in the case of unrestricted Gaussian diffusion. In biological tissue with its various compartments, membranes, etc., diffusion is restricted

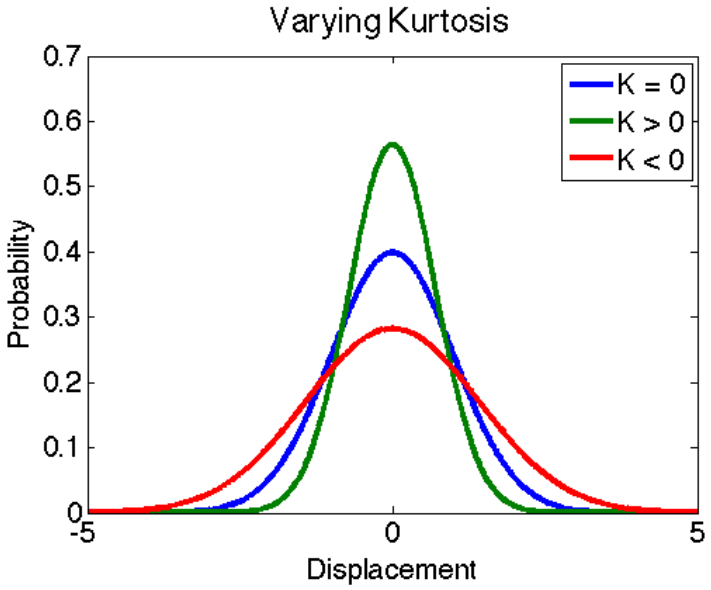

Figure 2. Distributions with different levels of kurtosis. Sample distributions are shown with K = 0 (blue), K < 0 (red), and K > 0 (green). The K = 0 distribution is a Gaussian distribution. The K < 0 distribution is platykurtic and less peaked than a Gaussian and the K > 0 distribution is leptokurtic and more peaked than a Gaussian. In biological tissue, K is almost always > 0 or more peaked than a Gaussian.

and Eq. 5 becomes an estimate:

$$S(b) \approx S_0 \exp(-bD), \quad [16]$$

where $S(b)$ is now used to explicitly indicate that the acquired signal is a function of b. This equation can be also re-written by taking the natural logarithm:

$$\ln[S(b)] \approx \ln(S_0) - bD. \quad [17]$$

Defined through the cumulant expansion of the diffusion MRI signal (33-36), an expanded form of Eq. 17 is:

$$\ln[S(b)] \approx \ln(S_0) - bD + \frac{1}{6}b^2D^2K + O(b^3), \quad [18]$$

where K is the diffusional kurtosis coefficient. If the chosen b-values are small enough so that the $O(b^3)$ term is negligible, then Eq. 18 is reduced to:

$$\ln[S(b)] \approx \ln(S_0) - bD + \frac{1}{6}b^2D^2K. \quad [19]$$

Using this signal equation, the kurtosis of the water diffusion displacement PDF can be estimated from DW-MRI acquisitions. This imaging method is known as diffusion kurtosis imaging or DKI and is a natural extension of DTI (18). Since b is pre-determined by the gradient parameters and $S(b)$ is measured, there are three unknowns in Eq. 19: S_0, D, and K. This means that at least three total b-values are required in order to estimate D and K in a single direction.

I.3.2 Calculation of the Kurtosis Tensor

Similar to the anisotropic behavior of diffusion in tissue, diffusion kurtosis is also direction dependent. However, instead of being described by a rank-2 tensor, diffusion kurtosis requires a symmetric rank-4 tensor with 81 total components (3x3x3x3), 15 of them being unique. Therefore, calculation of the kurtosis tensor requires measurements in at least 15 non-collinear, non-coplanar directions. The kurtosis tensor **W** or KT can be estimated from directional diffusion and kurtosis coefficients using the equation **(**18):

$$K(\boldsymbol{n}) = \frac{\overline{D}^2}{D(\boldsymbol{n})^2} \sum_{i,j,k,l=1}^{3} n_i n_j n_k n_l \, \boldsymbol{W}_{ijkl}, \qquad [20]$$

where $D(\boldsymbol{n})$ and $K(\boldsymbol{n})$ are the diffusion and kurtosis coefficients along a single direction, $\overline{D}$ (or MD) is the mean diffusivity, and n_i is a normalized diffusion gradient component for each direction. Only considering the 15 unique elements of the KT, Eq. 20 can be reduced to (19):

$$\begin{aligned} K(\boldsymbol{n}) = \frac{\overline{D}^2}{D(\boldsymbol{n})^2} [& n_1^4 \boldsymbol{W}_{1111} + n_2^4 \boldsymbol{W}_{2222} + n_3^4 \boldsymbol{W}_{3333} + 4(n_1^3 n_2 \boldsymbol{W}_{1112} \\ & + n_1^3 n_3 \boldsymbol{W}_{1113} + n_1 n_2^3 \boldsymbol{W}_{1222} + n_2^3 n_3 \boldsymbol{W}_{2223} + n_1 n_3^3 \boldsymbol{W}_{1333} \\ & + n_2 n_3^3 \boldsymbol{W}_{2333}) + 6(n_1^2 n_2^2 \boldsymbol{W}_{1122} + n_1^2 n_3^2 \boldsymbol{W}_{1133} + n_2^2 n_3^2 \boldsymbol{W}_{2233}) \\ & + 12(n_1^2 n_2 n_3 \boldsymbol{W}_{1123} + n_1 n_2^2 n_3 \boldsymbol{W}_{1223} + n_1 n_2 n_3^2 \boldsymbol{W}_{1233}). \end{aligned} \qquad [21]$$

Once the kurtosis tensor is calculated, then rotationally invariant kurtosis measures can be extracted.

Compared with the diffusion tensor, extracting useful measures from the kurtosis tensor is not necessarily as straightforward. However, one approach is to rotate the kurtosis tensor to the same reference frame as the diagonalized diffusion tensor:

$$\widetilde{\boldsymbol{W}}_{ijkl} = \sum_{i,j,k,l=1}^{3} R_{ii'} R_{jj'} R_{kk'} R_{ll'} \boldsymbol{W}_{i'j'k'l'}, \quad [22]$$

where R_{ij} is the jth component of the DT eigenvector corresponding to the eigenvalue λ_i. From this, parameters including mean kurtosis (MK), axial kurtosis (AK), and radial kurtosis (RK) can be determined. MK is the diffusional kurtosis averaged over all gradient directions and can be calculated as:

$$\begin{aligned} MK = {} & F_1(\lambda_1, \lambda_2, \lambda_3)\widetilde{\boldsymbol{W}}_{1111} + F_1(\lambda_2, \lambda_1, \lambda_3)\widetilde{\boldsymbol{W}}_{2222} + F_1(\lambda_3, \lambda_2, \lambda_1)\widetilde{\boldsymbol{W}}_{3333} \\ & + F_2(\lambda_1, \lambda_2, \lambda_3)\widetilde{\boldsymbol{W}}_{2233} + F_2(\lambda_2, \lambda_1, \lambda_3)\widetilde{\boldsymbol{W}}_{1133} \\ & + F_2(\lambda_3, \lambda_2, \lambda_1)\widetilde{\boldsymbol{W}}_{1122}, \end{aligned} \quad [23]$$

where $\widetilde{\boldsymbol{W}}_{ijkl}$ are components of the rotated kurtosis tensor and

$$\begin{aligned} F_1(\lambda_1, \lambda_2, \lambda_3) \equiv {} & \frac{(\lambda_1 + \lambda_2 + \lambda_3)^2}{18(\lambda_1 - \lambda_2)(\lambda_1 - \lambda_3)} \left[\frac{\sqrt{\lambda_2 \lambda_3}}{\lambda_1} R_F\left(\frac{\lambda_1}{\lambda_2}, \frac{\lambda_1}{\lambda_3}, 1\right) \right. \\ & \left. + \frac{3\lambda_1^2 - \lambda_1\lambda_2 - \lambda_1\lambda_3 - \lambda_2\lambda_3}{3\lambda_1\sqrt{\lambda_2\lambda_3}} R_D\left(\frac{\lambda_1}{\lambda_2}, \frac{\lambda_1}{\lambda_3}, 1\right) - 1 \right], \end{aligned} \quad [24]$$

and

$$F_2(\lambda_1,\lambda_2,\lambda_3) \equiv \frac{(\lambda_1+\lambda_2+\lambda_3)^2}{3(\lambda_2-\lambda_3)^2}\left[\frac{\lambda_2+\lambda_3}{\sqrt{\lambda_2\lambda_3}}R_F\left(\frac{\lambda_1}{\lambda_2},\frac{\lambda_1}{\lambda_3},1\right)\right.$$
$$\left.+\frac{2\lambda_1-\lambda_2-\lambda_3}{3\sqrt{\lambda_2\lambda_3}}R_D\left(\frac{\lambda_1}{\lambda_2},\frac{\lambda_1}{\lambda_3},1\right)-2\right], \quad [25]$$

where R_F and R_D represent Carlson's elliptic integrals (37).

AK corresponds to the kurtosis along the principal diffusion direction (ε_1) and is given by:

$$AK = \frac{(\lambda_1+\lambda_2+\lambda_3)^2}{9\lambda_1^2}\widetilde{\boldsymbol{W}}_{1111}. \quad [26]$$

RK is the mean diffusional kurtosis of all directions orthogonal to the principal diffusion direction and can be calculated with:

$$RK = G_1(\lambda_1,\lambda_2,\lambda_3)\widetilde{\boldsymbol{W}}_{2222} + G_1(\lambda_1,\lambda_3,\lambda_2)\widetilde{\boldsymbol{W}}_{3333} + G_2(\lambda_1,\lambda_2,\lambda_3)\widetilde{\boldsymbol{W}}_{2233}, \quad [27]$$

where

$$G_1(\lambda_1,\lambda_2,\lambda_3) \equiv \frac{(\lambda_1+\lambda_2+\lambda_3)^2}{18\lambda_2(\lambda_2-\lambda_3)^2}\left(2\lambda_2+\frac{\lambda_3^2-3\lambda_2\lambda_3}{\sqrt{\lambda_2\lambda_3}}\right), \quad [28]$$

and

$$G_2(\lambda_1,\lambda_2,\lambda_3) \equiv \frac{(\lambda_1+\lambda_2+\lambda_3)^2}{3(\lambda_2-\lambda_3)^2}\left(\frac{\lambda_2+\lambda_3}{\sqrt{\lambda_2\lambda_3}}-2\right). \quad [29]$$

Derivations of these equations can be found in Ref. 38. As shown above, calculation of the diffusion tensor is necessary for the calculation of the kurtosis tensor. Therefore, in addition to these kurtosis metrics, the diffusion tensor metrics MD, AD, RD, and FA can also be determined.

I.3.3 Considerations for Diffusion Kurtosis Imaging Protocols

As noted earlier, DTI requires a minimum of 7 acquisitions: 1 b=0 image and 1 non-zero b-value for at least 6 directions. In most cases, more than 6 directions are used in order to obtain a more precise estimate of the diffusion tensor, and therefore, improve the precision of extracted indices such as FA. Additionally, the b-value must be carefully chosen. If the high or non-zero b-value is too low, then the variation in signal between the b=0 image and high b-value image will be small and estimates of D will be more susceptible to noise. However, if the non-zero b-value is too high, then there will be greater contributions from the b^2 term (not present in the DTI model) and the measured value of D will be inaccurate. For in vivo brain DTI with $D \approx 1\ \mu m^2/ms$, the optimal b-value in order to maximize the precision and accuracy of the diffusion tensor is $\approx 1000\ s/mm^2$. A common clinical in vivo brain DTI protocol includes at least 1 b=0 image and b = 1000 for 30 directions. With data collected along more than 6 directions, the diffusion tensor can be estimated using a least-squares approach.

Since DKI utilizes a higher order model than conventional DTI and is therefore more susceptible to noise, care must be taken in establishing an appropriate imaging protocol. As described previously, at higher b-values, the DTI approximation breaks down. In the DKI model however, higher b-values are necessary for a precise

measurement of kurtosis, as its contribution to the MR signal is dependent on b^2. Similar to the DTI model, if the maximum b-value is too high, then contributions from the b^3 term will become more significant and errors in the estimates of D and K will result. Figure 3 shows the difference between fits based on the DTI and DKI signal equations

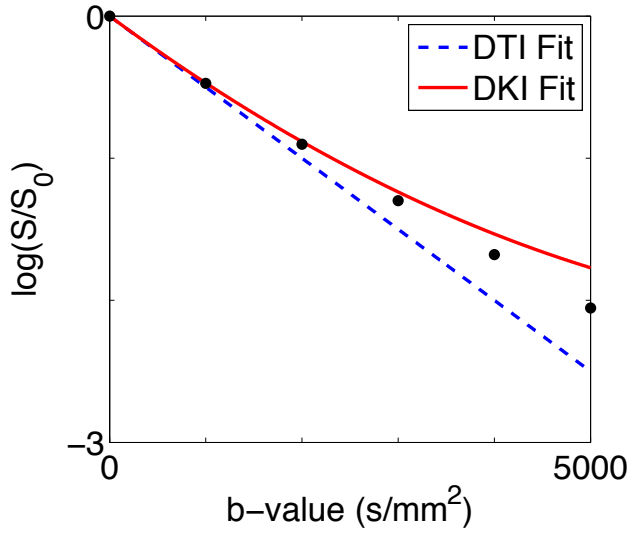

Figure 3. Comparison of signal fits for DTI and DKI models. Typical simulated data demonstrate the performance of the 1st and 2nd order signal models (or DTI and DKI models, respectively) as b-value increases. Notice that the DTI model performs well up to b-values of ≈ 1000 s/mm^2, but significantly worse as b-value increases. The DKI model performs better for b-values up to 2000-3000 s/mm^2.

for simulated data. If it is assumed that S(b) is a monotonically decreasing function (which is the case for biological tissue), then an upper bound for b can be obtained to ensure the validity of the DKI model (39):

$$b \leq \frac{3}{DK}. \qquad [30]$$

For typical in vivo values in the brain of D ≈ 1 μm^2/ms and K ≈ 1, the upper bound for b is 3000 s/mm^2. Empirical evidence suggests that the maximum b-value used for in vivo

brain studies should be between 2000 and 3000 s/mm^2 (20). If D or K is different, such as in other parts of the body or in ex vivo tissue samples, then the b-values must be adjusted accordingly. For example, in the ex vivo rat brain study presented in this work, non-zero b-values of 3000 and 6000 s/mm^2 were selected due to a much lower diffusion coefficient of ≈ 0.3 μm^2/ms.

As indicated previously, estimation of the kurtosis tensor requires the sampling of a minimum of 15 directions and at least two non-zero b-values per direction. In most cases, more than 15 directions are utilized to improve the precision of KT. More than 2 non-zero b-values per direction may also be used to allow for assessment of goodness-of-fit as well as increased precision of D and K at the expense of much longer scan times. If more than 15 directions are sampled, the kurtosis tensor can be estimated using a least-squares method. A typical in vivo brain DKI protocol includes at least 1 b=0 image and b = 1000 and 2000 for 30 directions, for a total of 61 or more acquired images or volumes. As with most diffusion MRI methods, there are trade-offs between the number of directions, number of b-values, image resolution, and acquisition time that must be considered when forming a DKI protocol.

I.4 Diffusion-Weighted Fast Spin-Echo

I.4.1 Conventional Fast Spin-Echo and the CPMG Conditions

Fast spin-echo (FSE) is an accelerated MRI sequence that utilizes an RF excitation pulse followed by multiple RF refocusing pulses to form multiple spin echoes (40,41). Using this method, multiple lines of k-space can be sampled after a single

excitation, making it much faster than a conventional spin-echo acquisition. For example, if 16 echoes are encoded each excitation, image acquisition will be 16 times faster than with a normal spin-echo sequence. The potential length of the echo train is limited by T_2 relaxation of the transverse magnetization and the time between echoes or echo spacing (ESP). Although generally slower than other accelerated MRI sequences, such as echo-planar imaging (EPI) or gradient and spin-echo (GRASE), FSE is less sensitive to off-resonance effects and is therefore preferred for high-resolution imaging. However, as with most accelerated imaging sequences, FSE also comes with various artifacts, such as blurring and ghosting.

Imperfect excitation and refocusing pulses will produce echoes that are out of phase with each other, and when acquired, cause signal loss and ghosting artifacts. In pulse sequences with multiple refocusing pulses, there are three types of echoes generated: primary spin echoes, stimulated echoes, and secondary spin echoes. Primary spin echoes (or just spin echoes) consist of spins that are excited and then experience a phase reversal every refocusing pulse. Spins from stimulated echoes are excited to the transverse plane, stored on the longitudinal plane by an imperfect refocusing pulse, and re-excited by an additional imperfect refocusing pulse. Secondary spin echoes are formed from spins that are excited by imperfect refocusing pulses and then phase-reversed by subsequent refocusing pulses. Crusher gradients are used to cancel out secondary spin echoes, since they will typically be out of phase with the primary spin echoes. Figure 4 shows signal coherence pathways generated by a fast spin-echo pulse sequence.

To prevent signal loss and ghosting artifacts, echoes should occur at the desired time in the sequence and echoes that occur at the same time should have the same phase.

A set of rules called the CPMG (Carr-Purcell-Meiboom-Gill) conditions (27,42) ensures that this happens. The first condition is that the refocusing pulses should be 90° out of

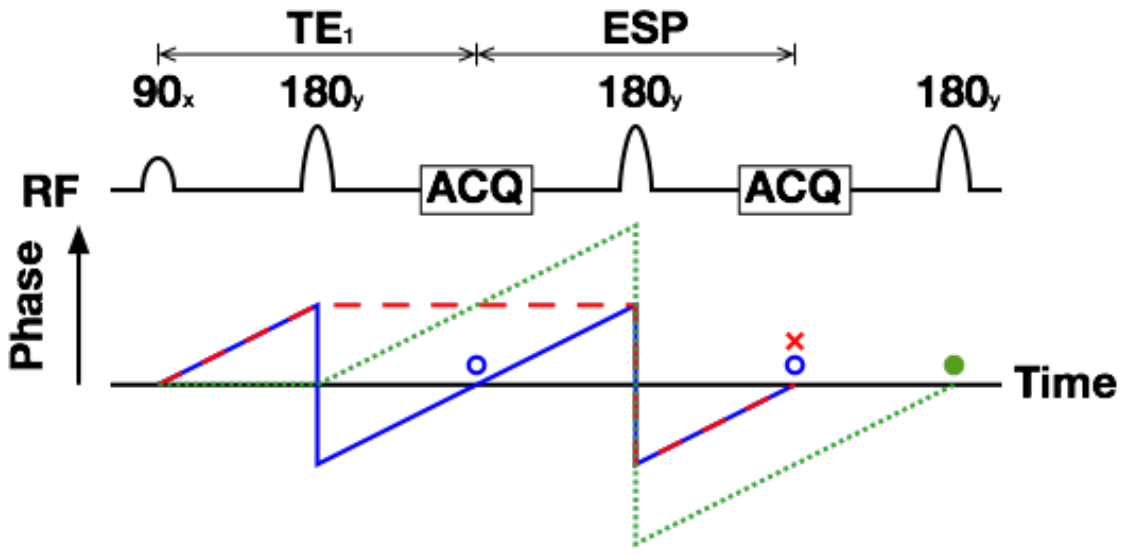

Figure 4. Signal coherence pathways of a typical fast spin-echo sequence. Primary spin-echo, stimulated echo, and secondary spin-echo pathways are represented by blue solid lines, red dashed lines, and green dotted lines, respectively. Temporal positions of primary spin echoes, stimulated echoes, and secondary spin echoes are denoted by blue circles, red x's, and green dots, respectively. In a CPMG fast spin-echo sequence, primary spin echoes and stimulated echoes will align temporally and have the same phase.

phase with the excitation pulse and be evenly spaced, meaning equal ESP throughout the echo train. The second condition is that the phase accumulated by a spin between consecutive refocusing pulses must be equal. This means that gradient pulses, such as crusher gradients and phase encoding gradients, must be equal in area on either side of the refocusing pulses, requiring phase encoding gradients to be rewound after each echo acquisition. If these two conditions are maintained, then the primary spin echoes and stimulated echoes coincide at the same time and have the same phase, minimizing signal loss and phase-induced artifacts.

I.4.2 Diffusion Weighting and non-CPMG Fast Spin-Echo

Due to the large amount of data acquired in typical diffusion-weighted scans, an accelerated sequence like FSE seems to be an optimal choice, yet combining DW-MRI and FSE is not exactly trivial. There are two main problems with incorporating diffusion-weighting gradients into an FSE sequence. First, the pair of diffusion-weighting gradients surrounding the first refocusing pulse violates the CPMG conditions and will cause phase errors between the primary spin echoes and stimulated echoes. Second, inserting PGSE diffusion weighting greatly extends the minimum echo time of the first echo, so maintaining an equal ESP throughout the sequence would not be practical due to T_2 relaxation. Since diffusion-weighting gradients inherently violate the CPMG conditions, other methods must be utilized for FSE to be suitable for diffusion-weighted imaging.

One solution to the problems that arise from diffusion-weighted FSE imaging is to mitigate contributions from the stimulated echoes and therefore minimize phase errors. This method still employs diffusion-weighting gradients straddling the first refocusing pulse, but also includes modulated crusher gradients to cancel out the signal from stimulated echoes (43). Crusher gradient amplitudes must change with each refocusing pulse, otherwise stimulated echoes will be rephased by crusher gradients later in the echo train rather than being continually dephased. Using this technique, the CPMG conditions can be violated without introducing additional artifacts or causing a major loss in signal. In this case, the pulse sequence is referred to as "non-CPMG fast spin-echo." Even though removal of the stimulated echoes results in a slight reduction in SNR, the non-CPMG FSE sequence still maintains higher SNR efficiency than a conventional spin-echo sequence, as well as allowing for the collection of more data in a reduced scan time.

Additionally, with cancellation of the stimulated echoes, the echo spacing can be shorter than the first echo time as spin echoes and stimulated echoes no longer need to align in the temporal domain. Typically, in a diffusion-weighted FSE sequence, TE_1 or TE will be much longer than ESP due to the inclusion of the diffusion-weighting gradients and diffusion time. With these modifications, diffusion-weighted FSE is a sequence especially useful for accelerated high-resolution diffusion-weighted imaging.

CHAPTER II

METHODS

II.1 Sample Preparation

All animal studies were completed with the approval of the Vanderbilt University Institutional Animal Care and Use Committee. Adult Sprague-Dawley rats were euthanized and transcardially perfusion-fixed with 2.5% glutaraldehyde and 2% paraformaldehyde + 1mM Gd-DTPA (Magnevist, Bayer HealthCare, Wayne, NJ, USA) in phosphate-buffered saline (PBS) (44,45). Then, rat brains were excised and post-fixed in the same fixative solution at 4°C for a period of 1 week to allow for complete penetration of the fixative. Afterwards, brain samples were placed in PBS + 1mM Gd-DTPA at 4°C for at least 1 week before imaging, with the solution changed out 2-3 times, in order to wash out residual fixative that reduces the tissue T_2 and image SNR (46). The addition of 1 mM Gd-DTPA lowered the T_1 of rat brain to ≈ 400 ms at 15.2T, effectively increasing the SNR efficiency of the MR acquisition. For imaging, rat brains were placed in MR-compatible tubes filled with a perfluropolyether liquid (Fomblin, Solvay Solexis, Thorofare, NJ, USA) for susceptibility matching, preventing tissue dehydration, and a signal-free background (47).

Once the imaging protocol was established, preliminary data were collected from rat brains after repeated injections of phencyclidine (PCP), a model of schizophrenia. For this study, male adult Sprague-Dawley rats were injected subcutaneously with 3 mg/kg of PCP (N=5) or saline (N=5) twice daily for 5 days. After the treatment period, the rats

were perfusion-fixed and the brains were prepared for imaging using the methods listed above.

II.2 MRI Acquisition

Imaging was performed on a 15.2T 11-cm horizontal bore Bruker BioSpec scanner (Bruker BioSpin, Billerica, MA, USA) using a Bruker 35-mm quadrature volume coil for RF transmission and reception. DKI data were acquired using an in-house developed 3D diffusion-weighted fast spin-echo sequence with TR/TE/ESP = 450/19.1/7.3 ms, ETL = 4, FOV = 24 x 16 x 12 mm^3, and matrix size = 96 x 64 x 48 for a 250 x 250 x 250 μm^3 isotropic resolution. For excitation and refocusing, non-selective hard pulses were implemented with durations of 125 and 250 μs, respectively. Crusher gradient pairs were modulated each refocusing pulse with amplitudes = 10, -10, 20, and -20 G/cm and durations = 1 ms. Receiver bandwidth for signal acquisition = 50 kHz. Pulsed gradient diffusion weighting was achieved with δ/Δ = 5/12 ms, prescribed b-

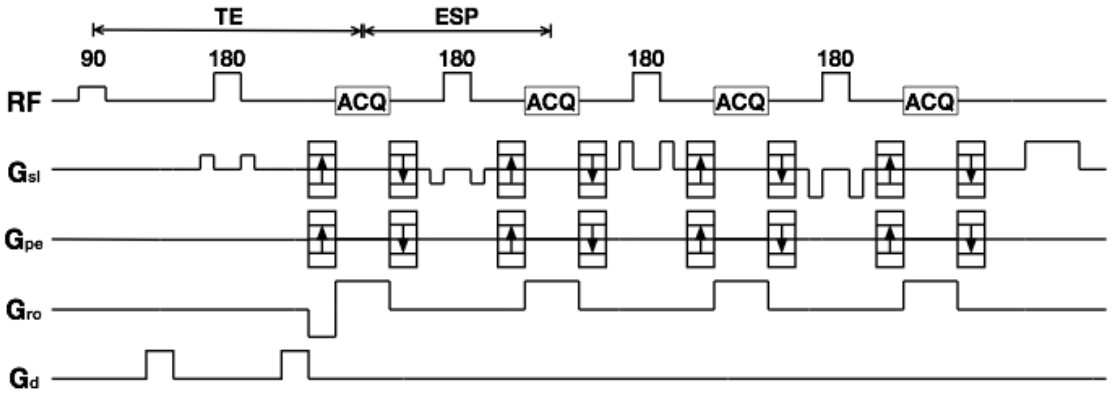

Figure 5. Diffusion-weighted FSE pulse sequence diagram. G_{sl}, G_{pe}, and G_{ro} denote gradient waveforms along the slice, phase, and readout axes, respectively. G_d represents the diffusion gradient pulses. In this sequence, ESP is shorter than TE. Phase encoding gradients are rewound after the acquisition of each echo. Crusher gradient pair amplitudes are different for each refocusing pulse. Gradient pulse amplitudes and durations are not necessarily to scale.

values = 3000 and 6000 s/mm^2, 30 directions, and 2 signal averages with gradient polarity reversal to mitigate background gradient cross-terms. 5 b=0 images were collected and averaged to improve the precision of DKI fits. Therefore, 125 3D volumes were collected in a total scan time of ≈ 12 hours. Figure 5 shows a diagram of the diffusion-weighted fast spin-echo pulse sequence.

II.3 Data Analysis

Image data were analyzed using in-house written code in Matlab (Mathworks, Natick, MA, USA). During reconstruction from the k-space data, 3D image volumes were zero-padded x2 in each direction. Then, b=0 images were averaged and diffusion-weighted images with opposite gradient polarities were geometrically averaged to reduce contributions from background gradient cross-terms (48). Next, diffusion and kurtosis tensors were estimated voxel-wise using a constrained linear least-squares approach (38). From these tensors, DTI indices FA, MD, AD, and RD and DKI indices MK, AK, and RK were calculated on a voxel-wise basis.

For the PCP rat model, group analysis was performed to evaluate the effects of the PCP treatments on DKI parameters. After diffusion and kurtosis tensors were estimated and DTI and DKI parameter maps were calculated, b=0 images were registered to a chosen template brain using a rigid affine registration. Additional registration of the b=0 images was performed using a non-rigid deformable demons registration (49). Afterwards, DTI and DKI parameter maps of each brain were registered using the same transformations derived from the b=0 registrations. From these, group-averaged parameter maps were formed. ROIs for 2 gray matter structures: cerebral cortex (CT) and

caudate putamen (CPu), and 3 white matter structures: corpus callosum (CC), external capsule (EC), and the fimbria of the hippocampus (FI), were manually delineated on axial cross-sections. Group comparisons of DTI and DKI indices were made for these ROIs using the Wilcoxon rank-sum test, which tests for the equality of medians between two groups (50).

CHAPTER III

RESULTS

Typical white matter SNR of the b=0 image was ~370, providing intrinsic precision of DTI and DKI parameters better than 3.1% coefficient of variation in all cases. Figures 6-8 show axial, coronal, and sagittal cross-sections of DTI and DKI parameter maps in a normal rat brain. As expected, strong contrast between white and gray matter structures is seen in the RD, FA, MK, and RK parameter maps. Additionally, the values of DTI and DKI parameters in main structures are similar to those previously reported in a 2D multi-slice ex vivo rat brain DKI study (21).

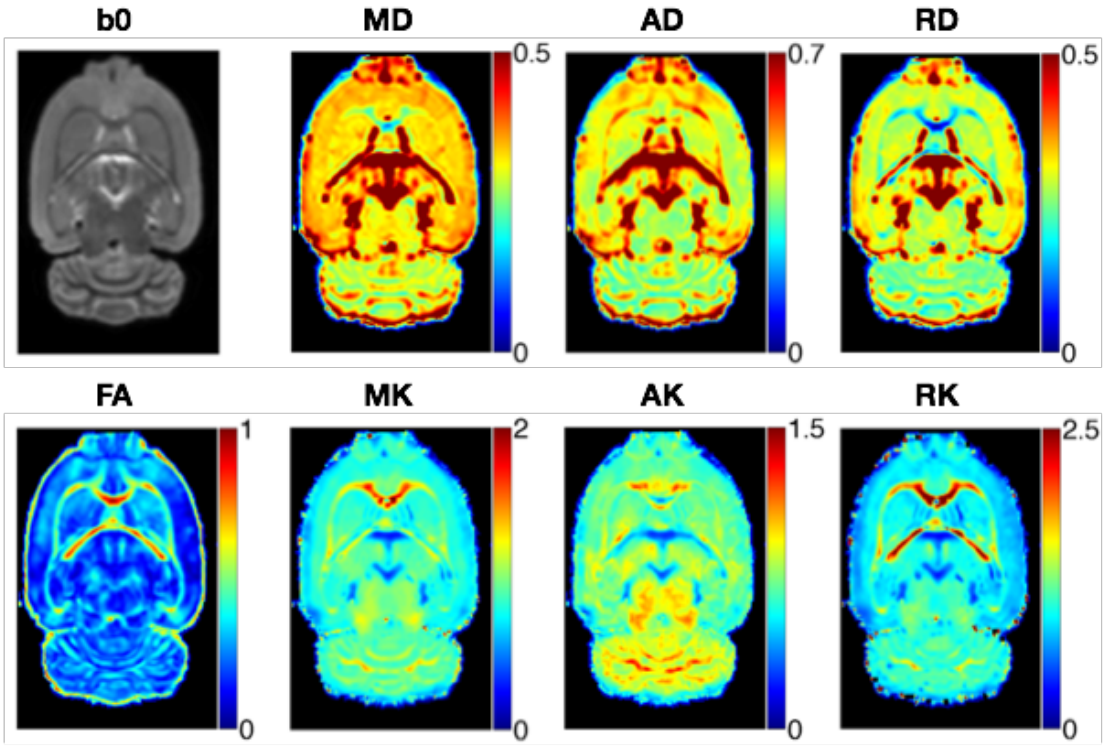

Figure 6. Axial cross-section DTI and DKI parameter maps of a normal rat brain. MD, AD, and RD are in units of $\mu m^2/ms$. FA, MK, AK, and RK are dimensionless.

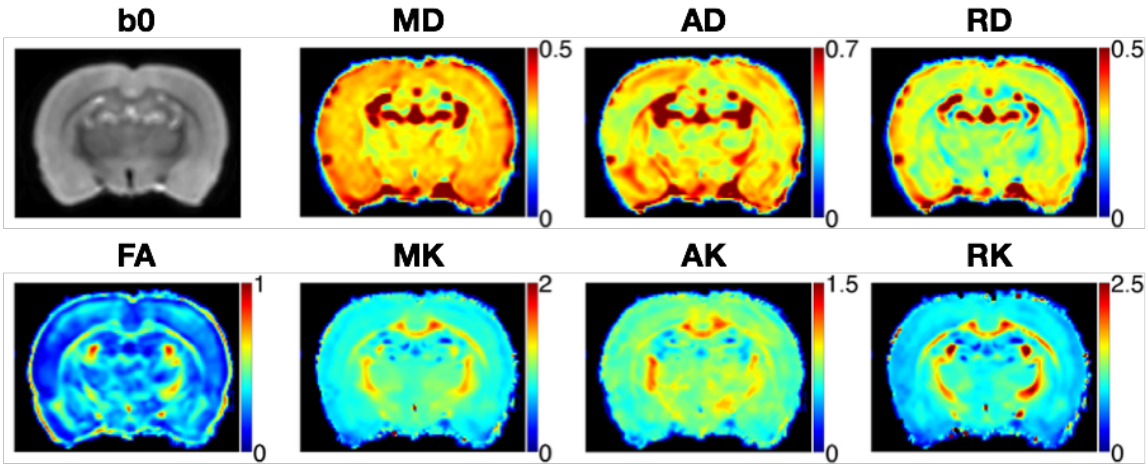

Figure 7. Coronal cross-section DTI and DKI parameter maps of a normal rat brain. MD, AD, and RD are in units of $\mu m^2/ms$. FA, MK, AK, and RK are dimensionless.

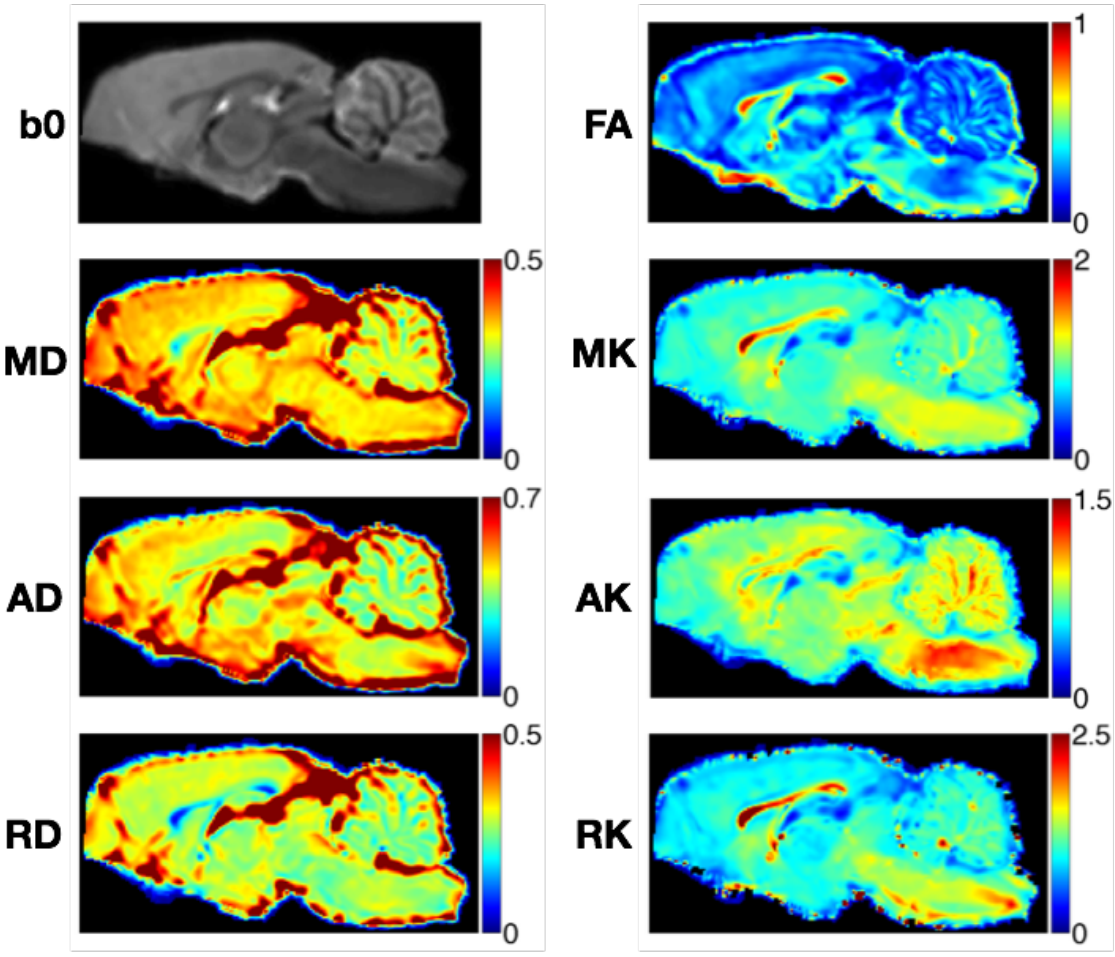

Figure 8. Sagittal cross-section DTI and DKI parameter maps of a normal rat brain. MD, AD, and RD are in units of $\mu m^2/ms$. FA, MK, AK, and RK are dimensionless.

From the imaging study of the PCP rat model, Table 1 shows the DTI and DKI parameter means and standard deviations for each group in 5 ROIs. The PCP-treated group exhibited a significant increase in MK and AK of the external capsule ($p < 0.05$). Significant differences were not observed for any parameter in the other chosen ROIs. Figure 9 shows axial cross-sections of group-averaged DTI and DKI parameter maps for both the control and PCP groups.

Table 1. DTI and DKI parameter ROI means in control and PCP-treated rat brains. Group mean ± standard deviation of FA, MD, AD, RD, MK, AK, and RK for 5 ROIs: CT = cerebral cortex, CPu = caudate putamen, CC = corpus callosum, EC = external capsule, and FI = fimbria of the hippocampus. * indicates $p < .05$ from the Wilcoxon rank-sum test. MD, AD, and RD are in units of $\mu m^2/ms$. FA, MK, AK, and RK are dimensionless.

		CT	CPu	CC	EC	FI
FA	**Con**	**0.23±.03**	**0.29±.03**	**0.86±.07**	**0.42±.03**	**0.67±.03**
	PCP	**0.23±.02**	**0.28±.04**	**0.82±.06**	**0.44±.02**	**0.67±.08**
MD	**Con**	**0.34±.02**	**0.32±.02**	**0.22±.06**	**0.33±.02**	**0.39±.03**
	PCP	**0.33±.01**	**0.31±.01**	**0.23±.03**	**0.31±.01**	**0.37±.03**
AD	**Con**	**0.42±.04**	**0.41±.02**	**0.53±.16**	**0.48±.02**	**0.75±.09**
	PCP	**0.41±.01**	**0.40±.01**	**0.52±.10**	**0.47±.01**	**0.69±.02**
RD	**Con**	**0.29±.01**	**0.27±.02**	**0.06±.02**	**0.25±.02**	**0.21±.01**
	PCP	**0.29±.01**	**0.27±.01**	**0.08±.02**	**0.23±.01**	**0.20±.05**
MK	**Con**	**0.81±.03**	**0.84±.03**	**1.45±.34**	**1.02±.04***	**1.14±.11**
	PCP	**0.81±.02**	**0.83±.04**	**1.25±.26**	**1.12±.05***	**1.15±.04**
AK	**Con**	**0.74±.02**	**0.73±.03**	**0.53±.09**	**0.83±.01***	**0.64±.05**
	PCP	**0.76±.02**	**0.71±.05**	**0.57±.07**	**0.91±.04***	**0.66±.04**
RK	**Con**	**0.87±.05**	**0.95±.03**	**1.65±1.21**	**1.30±.07**	**2.15±.17**
	PCP	**0.89±.03**	**0.92±.06**	**1.34±.84**	**1.43±.09**	**2.20±.16**

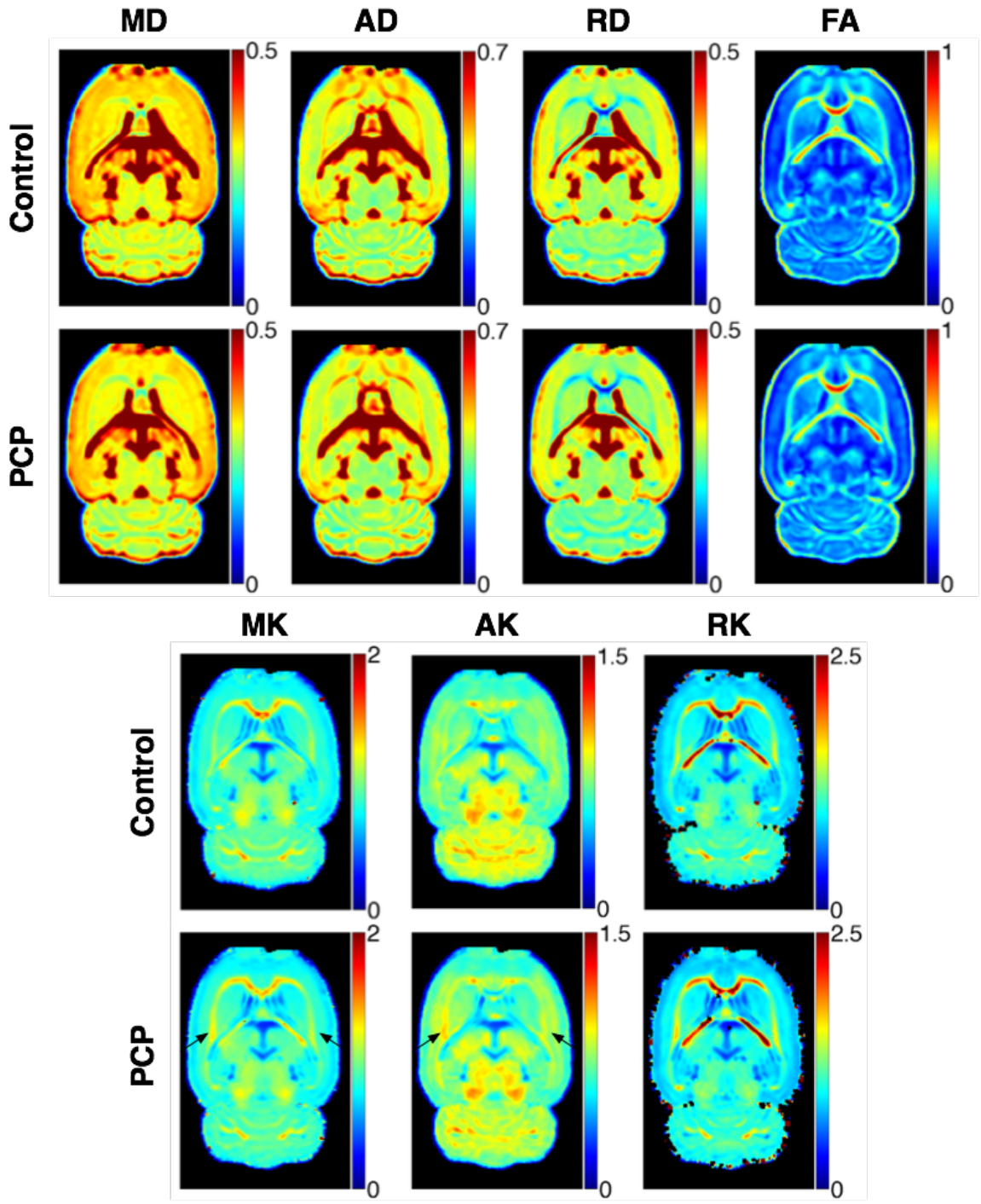

Figure 9. Axial cross-sections of group-averaged DTI and DKI parameter maps comparing control and PCP-treated groups. Increases in MK and AK of the external capsule in the PCP group are indicated with black arrows. MD, AD, and RD are in units of $\mu m^2/ms$. FA, MK, AK, and RK are dimensionless.

CHAPTER IV

DISCUSSION AND CONCLUSIONS

In this work, a protocol was developed for overnight high-resolution and high-precision 3D DKI of ex vivo rat brain. This protocol will be used to evaluate a variety of rodent neurological models through the detection of microstructural changes and assess the efficacy of potential treatments. In normal rat brain, areas of closely aligned axon bundles, such as in the corpus callosum, exhibit low radial diffusivity and high fractional anisotropy, mean kurtosis, and radial kurtosis, signifying a close relationship between these measures and white matter microstructure. With the high-resolution 3D imaging protocol, partial-volume effects were limited, allowing for improved DKI assessment of various white matter tracts. The resolution provided by this protocol was sufficient for evaluating the main white matter tracts in the brain, such as the corpus callosum, fornix, internal capsule, external capsule, and others. Even higher resolution would be needed to accurately quantify smaller white matter regions, such as cerebellar white matter. Additionally, the high SNR of this protocol allowed for excellent precision of DKI-derived parameters.

Many factors had to be considered during the formation of the DKI protocol. First, even though the imaged brains were ex vivo, scan time was limited to 12 hours in order to make the imaging of larger sample sizes more practical. In order to reduce scan time and maximize SNR, samples were immersed in gadolinium to reduce tissue T_1 and thereby allow for shorter repetition times without significantly decreasing SNR. A fast

spin-echo acquisition was utilized to enable additional data collection at an optimal repetition time in the allotted 12 hours. Due to the shortened T_2 (~30 ms) of tissue at 15.2T, the ETL of the acquisition was limited to 4 echoes, as additional echoes caused an unacceptable amount of T2-induced blurring. Furthermore, due to stronger background gradients present at 15.2T, mitigation of background gradient cross-terms was required in order to maintain the accuracy of DKI parameters, therefore doubling the amount of data that needed to be acquired. Also, due to decreased diffusivity in the brain tissue caused by chemical fixation, larger non-zero b-values of 3000 and 6000 s/mm^2 were necessary. Overall, protocol parameters were optimized to allow for high-resolution, high-precision 3D DKI of ex vivo rat brain at 15.2T.

The developed protocol was applied for the acquisition of preliminary data from the PCP schizophrenia rat model. Although changes in DKI metrics were not widespread, there were significant increases in MK and AK, but not RK, of the external capsule. Significant changes were not observed with conventional DTI metrics, indicating an increased sensitivity of DKI for detection of subtler changes in white matter microstructure. Although there are multiple underlying changes in white matter microstructure that affect diffusion parameters, it has been previously hypothesized that changes in diffusivity or kurtosis in the axial direction can be attributed to a change in axon structure. In this case, AK increased significantly, possibly indicating that the axons were damaged, causing diffusion restrictions along the axons. Histological evaluation of these brains would provide useful insight into the microstructural changes that are causing a change in diffusional kurtosis in the external capsule. Changes in the external capsule were not originally anticipated, yet the collection of whole-brain 3D imaging data

allowed for the evaluation of multiple brain structures and the discovery of these differences. This indicates the importance of a whole-brain 3D DKI protocol for evaluating neurological models and tracking potential treatments. Future directions for this project include an increased sample size and the inclusion of histological evaluation of the brain tissue for the purpose of correlating changes in DKI metrics with changes in white matter microstructure. Additionally, development of a high-resolution in vivo DKI protocol would be useful for serial tracking of potential treatments in this model as well as other rodent models of neurological diseases.

DKI has been shown to exhibit increased sensitivity to microstructural changes in both gray and white matter for a variety of disorders and diseases. Although this may be useful for the detection of white matter pathologies, specifying what exactly is causing these changes in water diffusion has proven to be more difficult. Performing DKI along with histological evaluation could lead to a better understanding of how DKI-derived metrics relate to white matter microstructure. With this knowledge, more accurate diagnoses would be possible as well as improved assessment of treatments.

In summary, a high-resolution, high-precision 3D DKI protocol for ex vivo rat brain was developed. Additionally, application of this protocol to a rat schizophrenia model is currently ongoing. Future directions involve the application of DKI to a variety of rodent neurological models in combination with histological assessment to determine the relationship between DKI and white matter microstructure.

REFERENCES

1. Hursh JB. Conduction velocity and diameter of nerve fibers. American Journal of Physiology. 1939;127:131–139.

2. Waxman SG. Determinants of conduction velocity in myelinated nerve fibers. Muscle & Nerve. 1980;3(2):141–150.

3. Kutzelnigg A. Cortical demyelination and diffuse white matter injury in multiple sclerosis. Brain. 2005;128(11):2705–2712.

4. Davis KL, Stewart DG, Friedman JI, Buchsbaum M, Harvey PD, Hof PR, Buxbaum J, Haroutunian V. White Matter Changes in Schizophrenia: Evidence for Myelin-Related Dysfunction. Archives of General Psychiatry. 2003;60(5):443–456.

5. Moseley ME, Cohen Y, Mintorovitch J, Chileuitt L, Shimizu H, Kucharczyk J, Wendland MF, Weinstein PR. Early detection of regional cerebral ischemia in cats: Comparison of diffusion- and T2-weighted MRI and spectroscopy. Magnetic Resonance in Medicine. 1990;14(2):330–346.

6. Mintorovitch J, Moseley ME, Chileuitt L, Shimizu H, Cohen Y, Weinstein PR. Comparison of diffusion- and T2-weighted MRI for the early detection of cerebral ischemia and reperfusion in rats. Magnetic Resonance in Medicine. 1991;18(1):39–50.

7. Baird AE, Warach S. Magnetic resonance imaging of acute stroke. Journal of Cerebral Blood Flow & Metabolism. 1998;18(6):583–609.

8. Larsson H, Thomsen C, Frederiksen J, Stubgaard M, Henriksen O. In vivo magnetic resonance diffusion measurement in the brain of patients with multiple sclerosis. Magnetic Resonance Imaging. 1992;10(1):7–12.

9. Filippi M, Cercignani M, Inglese M, Horsfield MA, Comi G. Diffusion tensor magnetic resonance imaging in multiple sclerosis. Neurology. 2001;56(3):304–311.

10. Kubicki M, McCarley R, Westin C, Park H, Maier S, Kikinis R, Jolesz F, Shenton M. A review of diffusion tensor imaging studies in schizophrenia. Journal of Psychiatric Research. 2007;41(1-2):15–30.

11. Alexander AL, Lee JE, Lazar M, Boudos R, DuBray MB, Oakes TR, Miller JN, Lu J, Jeong E-K, McMahon WM, et al. Diffusion tensor imaging of the corpus callosum in Autism. NeuroImage. 2007;34(1):61–73.

12. Rose SE, Chen F, Chalk JB, Zelaya FO, Strugnell WE, Benson M, Semple J, Doddrell DM. Loss of connectivity in Alzheimer's disease: an evaluation of white matter tract integrity with colour coded MR diffusion tensor imaging. Journal of Neurology, Neurosurgery & Psychiatry. 2000;69(4):528–530.

13. Basser PJ, Mattiello J, LeBihan D. Estimation of the Effective Self-Diffusion Tensor from the NMR Spin Echo. Journal of Magnetic Resonance, Series B. 1994;103(3):247–254.

14. Basser PJ, Mattiello J, LeBihan D. MR diffusion tensor spectroscopy and imaging. Biophysical Journal. 1994;66(1):259–267.

15. Le Bihan D, Mangin JF, Poupon C, Clark CA, Pappata S, Molko N, Chabriat H. Diffusion tensor imaging: concepts and applications. Journal of Magnetic Resonance Imaging. 2001;13(4):534–546.

16. Basser PJ, Jones DK. Diffusion-tensor MRI: theory, experimental design and data analysis–a technical review. NMR in Biomedicine. 2002;15(7-8):456–467.

17. Beaulieu C. The basis of anisotropic water diffusion in the nervous system - a technical review. NMR in Biomedicine. 2002;15(7-8):435–455.

18. Jensen JH, Helpern JA, Ramani A, Lu H, Kaczynski K. Diffusional kurtosis imaging: The quantification of non-gaussian water diffusion by means of magnetic resonance imaging. Magnetic Resonance in Medicine. 2005;53(6):1432–1440.

19. Lu H, Jensen JH, Ramani A, Helpern JA. Three-dimensional characterization of non-gaussian water diffusion in humans using diffusion kurtosis imaging. NMR in Biomedicine. 2006;19(2):236–247.

20. Jensen JH, Helpern JA. MRI quantification of non-Gaussian water diffusion by kurtosis analysis. NMR in Biomedicine. 2010;23(7):698–710.

21. Hui ES, Cheung MM, Qi L, Wu EX. Towards better MR characterization of neural tissues using directional diffusion kurtosis analysis. NeuroImage. 2008;42(1):122-134

22. Cheung MM, Hui ES, Chan KC, Helpern JA, Qi L, Wu EX. Does diffusion kurtosis imaging lead to better neural tissue characterization? A rodent brain maturation study. NeuroImage. 2009;45(2):386–392.

23. Ramani A, Jensen JH, Szulc KU, Ali O, Hu C, Lu H, Brodle JD, Helpern JA. Assessment of abormalities in the cerebral microstructure of schizophrenia patiens: a diffusional kurtosis imaging study. In Proceedings of the 15th Annual Meeting of ISMRM, Berlin, Germany. 2007;648.

24. Helpern JA, Adisetiyo V, Falangola MF, Hu C, Di Martino A, Williams K, Castellanos FX, Jensen JH. Preliminary evidence of altered gray and white matter microstructural development in the frontal lobe of adolescents with attention-deficit hyperactivity disorder: A diffusional kurtosis imaging study. Journal of Magnetic Resonance Imaging. 2011;33(1):17–23.

25. Einstein A. On the movement of small particles suspended in stationary liquids required by the molecular-kinetic theory of heat. Annalen der Physik. 1905;17(549-560):16.

26. Le Bihan D, Breton E, Lallemand D, Grenier P, Cabanis E, Laval-Jeantet M. MR imaging of intravoxel incoherent motions: application to diffusion and perfusion in neurologic disorders. Radiology. 1986;161(2):401–407.

27. Carr HY, Purcell EM. Effects of diffusion on free precession in nuclear magnetic resonance experiments. Physical Review. 1954;94(3):630.

28. Stejskal EO, Tanner JE. Spin Diffusion Measurements: Spin Echoes in the Presence of a Time-Dependent Field Gradient. The Journal of Chemical Physics. 1965;42(1):288.

29. Mori S, Crain BJ, Chacko VP, van Zijl PCM. Three-dimensional tracking of axonal projections in the brain by magnetic resonance imaging. Annals of Neurology. 1999;45(2):265–269.

30. Basser PJ, Pajevic S, Pierpaoli C, Duda J, Aldroubi A. In vivo fiber tractography using DT-MRI data. Magnetic Resonance in Medicine. 2000;44(4):625–632.

31. Basser PJ. Inferring microstructural features and the physiological state of tissues from diffusion-weighted images. NMR in Biomedicine. 1995;8(7):333–344.

32. DeCarlo LT. On the meaning and use of kurtosis. Psychological Methods. 1997;2(3):292.

33. Tanner JE. Transient diffusion in a system partitioned by permeable barriers. Application to NMR measurements with a pulsed field gradient. The Journal of Chemical Physics. 1978;69(4):1748.

34. Mitra PP, Sen PN. Effects of microgeometry and surface relaxation on NMR pulsed-field-gradient experiments: Simple pore geometries. Physical Review B. 1992;45(1):143.

35. Liu C, Bammer R, Acar B, Moseley ME. Characterizing non-gaussian diffusion by using generalized diffusion tensors. Magnetic Resonance in Medicine. 2004;51(5):924–937.

36. Frøhlich AF, Østergaard L, Kiselev VG. Effect of impermeable boundaries on diffusion-attenuated MR signal. Journal of Magnetic Resonance. 2006;179(2):223–233.

37. Carlson BC. Computing elliptic integrals by duplication. Numerische Mathematik. 1979;33(1):1–16.

38. Tabesh A, Jensen JH, Ardekani BA, Helpern JA. Estimation of tensors and tensor-derived measures in diffusional kurtosis imaging. Magnetic Resonance in Medicine. 2010;65(3):823–836.

39. Lazar M, Jensen JH, Xuan L, Helpern JA. Estimation of the orientation distribution function from diffusional kurtosis imaging. Magnetic Resonance in Medicine. 2008;60(4):774–781.

40. Hennig J, Nauerth A, Friedburg H. RARE imaging: a fast imaging method for clinical MR. Magnetic Resonance in Medicine. 1986;3(6):823–833.

41. Hennig J. Multiecho imaging sequences with low refocusing flip angles. Journal of Magnetic Resonance. 1988;78(3):397–407.

42. Meiboom S, Gill D. Modified Spin-Echo Method for Measuring Nuclear Relaxation Times. Review of Scientific Instruments. 1958;29(8):688.

43. Beaulieu CF, Zhou X, Cofer GP, Johnson GA. Diffusion-weighted MR microscopy with fast spin-echo. Magnetic Resonance in Medicine. 1993;30(2):201–206.

44. Karnovsky MJ. A formaldehyde-glutaraldehyde fixative of high osmolality for use in electron microscopy. Journal of Cell Biology. 1965;27:137A–138A.

45. Johnson GA, Cofer GP, Gewalt SL, Hedlund LW. Morphologic Phenotyping with MR Microscopy: The Visible Mouse. Radiology. 2002;222(3):789–793.

46. Shepherd TM, Thelwall PE, Stanisz GJ, Blackband SJ. Aldehyde fixative solutions alter the water relaxation and diffusion properties of nervous tissue. Magnetic Resonance in Medicine. 2009;62(1):26–34.

47. Benveniste H, Kim K, Zhang L, Johnson GA. Magnetic Resonance Microscopy of the C57BL Mouse Brain. NeuroImage. 2000;11(6):601–611.

48. Neeman M, Freyer JP, Sillerud LO. A simple method for obtaining cross-term-free images for diffusion anisotropy studies in NMR microimaging. Magnetic Resonance in Medicine. 1991;21(1):138–143.

49. Thirion JP. Image matching as a diffusion process: an analogy with Maxwell's demons. Medical image analysis. 1998;2(3):243-260.

50. Wilcoxon F. Individual comparisons by ranking methods. Biometrics. 1945;1(6):80–83.